PET image reconstruction with a system matrix containing point spread function derived from single photon incidence response*

Fan Xin(樊 馨)[a)b)], Wang Hai-Peng(王海鹏)[a)b)], Yun Ming-Kai(贠明凯)[a)c)], Sun Xiao-Li(孙校丽)[a)b)], Cao Xue-Xiang(曹学香)[a)c)], Liu Shuang-Quan(刘双全)[a)c)], Chai Pei(柴 培)[a)c)], Li Dao-Wu(李道武)[a)c)], Liu Bao-Dong(刘宝东)[a)c)], Wang Lu(王 璐)[a)b)], and Wei Long(魏 龙)[a)c)†]

[a)] *Key Laboratory of Nuclear Analytical Techniques, Institute of High Energy Physics, Chinese Academy of Sciences, Beijing* 100049, *China*
[b)] *University of Chinese Academy of Sciences, Beijing* 100049, *China*
[c)] *Beijing Engineering Research Center of Radiographic Techniques and Equipment, Beijing* 100049, *China*

(Received 18 June 2014; revised manuscript received 11 September 2014; published online 25 November 2014)

A point spread function (PSF) for the blurring component in positron emission tomography (PET) is studied. The PSF matrix is derived from the single photon incidence response function. A statistical iterative reconstruction (IR) method based on the system matrix containing the PSF is developed. More specifically, the gamma photon incidence upon a crystal array is simulated by Monte Carlo (MC) simulation, and then the single photon incidence response functions are calculated. Subsequently, the single photon incidence response functions are used to compute the coincidence blurring factor according to the physical process of PET coincidence detection. Through weighting the ordinary system matrix response by the coincidence blurring factors, the IR system matrix containing the PSF is finally established. By using this system matrix, the image is reconstructed by an ordered subset expectation maximization (OSEM) algorithm. The experimental results show that the proposed system matrix can substantially improve the image radial resolution, contrast, and noise property. Furthermore, the simulated single gamma-ray incidence response function depends only on the crystal configuration, so the method could be extended to any PET scanner with the same detector crystal configuration.

Keywords: point spread function, single photon incidence, system matrix, positron emission tomography

PACS: 87.57.nf, 87.57.uk, 87.57.C– **DOI:** 10.1088/1674-1056/24/1/018702

1. Introduction

Positron emission tomography (PET) is a nuclear medical imaging technique that provides important information for disease diagnosis, therapeutic effect assessment, and new drug development.[1] The PET system detects pairs of back to back gamma photons emitted indirectly from a positron-emitting radionuclide, which is injected into the living body on a biologically active tracer. The image of tracer concentration within the living body can be acquired by image reconstruction methods such as analytic reconstruction[2] and statistical iterative reconstruction (IR).[3] High quality PET imaging is vital to successful disease diagnosis and treatment evaluation. Quality includes image resolution, contrast, noise property, and so on.[4] The image resolution, which is crucial for the diagnosis of an early stage tumor, depends mainly on several factors such as the size of the detector, photon non-colinearity, the positron range, and the inter-crystal penetration.[5–8] The size of the detector may not be changed in an existing system. Among the other physical and geometric factors, the crystal penetration will lead to depth-of-interaction (DOI) blurring. The image spatial resolution degradation and positional error become more serious as the DOI blurring increases.[9] These physical and geometric factors can be accurately modeled by the system matrix in the IR reconstruction.[8]

Traditionally, the system matrix can be divided into components such as the geometrical component, the blurring component, and so on. A point spread function (PSF) is generally used to describe the blurring component. The PSF can be modeled by analytic methods,[10–12] Monte Carlo (MC) simulation methods,[13–15] and experimental methods.[16–22] It requires a huge amount of work to obtain the spatially variant PSFs[23] of all the voxels in the experiment,[19] in which purely analytic methods are less accurate than the other methods.[19,20] Several studies have proposed methods that first obtain a few specific PSFs by experimental measurements or MC simulations and then use specific models (for example the Gaussian function model[19] or iterative algorithm[22]) to estimate the PSFs of all the voxels based on the system symmetry.[19,20,22] Thus, the experimental time is reduced dramatically. However, it is improper for an accurate system model to model only radial blurring while ignoring azimuthal blurring,[19,20] a fatal flaw in most of these methods. Moreover, it is tedious that in these methods, more than one experiment or simulation needs to be carried out in order to cover the geometrical structures of different PET scanners.[19,20]

In this paper, we propose a new method which calculates the PSF information based on the single gamma photon incidence response function. The PET imaging theory is intro-

*Project supported by the National Natural Science Foundation of China (Grant Nos. Y4811H805C and 81101175).
†Corresponding author. E-mail: weil@ihep.ac.cn
© 2015 Chinese Physical Society and IOP Publishing Ltd

duced in Section 2. The new method is introduced in Section 3. The improved results and corresponding analysis are given in Section 4. Finally, in Section 5, some related problems are discussed.

2. PET imaging theory

In IR methods, the system matrix describes the relationship between projection and image space. This relationship can be expressed as

$$p_j = \sum_i a_{ij} f_i, \tag{1}$$

where p_j is the true value of the projection data for a line of response (LOR) detected by the detector pair j; f_i is the value of the image at voxel i; and a_{ij} is the probability of detecting a coincidence event originating from voxel i at detector pair j.[19] We define $\boldsymbol{A}$ as the matrix of a_{ij}. So $\boldsymbol{A}$ represents the system matrix, which can be divided into several factored matrices.[19] It can be expressed as

$$\boldsymbol{A} = \boldsymbol{A}_{\text{sens}} \boldsymbol{A}_{\text{atten}} \boldsymbol{A}_{\text{blur}} \boldsymbol{A}_{\text{geom}} \boldsymbol{A}_{\text{positron}}. \tag{2}$$

The positron range factor $\boldsymbol{A}_{\text{positron}}$ is relatively smaller and can be ignored for ^{18}F.[24] The attenuation factor $\boldsymbol{A}_{\text{atten}}$ can be provided by an extra CT scan,[25] and the detector sensitivity factor $\boldsymbol{A}_{\text{sens}}$ can be acquired by measuring a uniform cylindrical source.[26] The remaining factors are the geometrical factor $\boldsymbol{A}_{\text{geom}}$ and the blurring factor $\boldsymbol{A}_{\text{blur}}$.[27] The geometrical factor can be accurately estimated by analytical methods such as the line integral model,[28] the tube model,[29] and the solid angle model.[19,30] However, owing to the complicated response, it is always difficult to acquire an accurate blurring factor. The method should accommodate physical effects such as crystal penetration and photon non-colinearity[5–8] which would result in the degradation of the reconstructed image quality, as mentioned before.

3. PSF modeling method

3.1. Monte Carlo simulation for single photon incidence response function

Generally, a modern PET scanner uses uniform detector blocks and has a polygonal shape. Each block consists of a crystal array to which a number (usually four) of photomultiplier tubes are attached. Figure 1 shows the PET structure and the block structure.

For a PET system, the blurring effect refers mainly to DOI blurring. DOI blurring results from crystal penetration, which is caused by non-normal incidence of the gamma-ray.[9] The bigger the angle of incidence is, the more serious the DOI blurring is.[31] Figure 2 displays three different incidence patterns of gamma-ray incidence at the detector array. In Fig. 2(a), a few crystals are being penetrated at normal incidence. In Figs. 2(b) and 2(c), the gamma-ray may penetrate a few adjacent crystals at non-normal incidence. For the same crystal configuration, the gamma-ray's penetration of adjacent crystal is decided mainly by the incidence angle.[31] In Fig. 2(b), two crystals are penetrated, while in Fig. 2(c) where the incidence angle is larger, three crystals are penetrated. Theoretically, because the blocks in PET are uniform, the responses of all blocks are the same. So, we need only study the responses of all incidence angles for a single block.

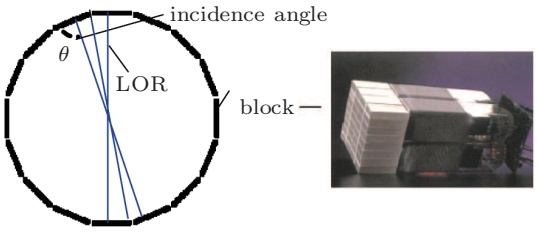


Fig. 1. (color online) PET structure and one of its blocks.

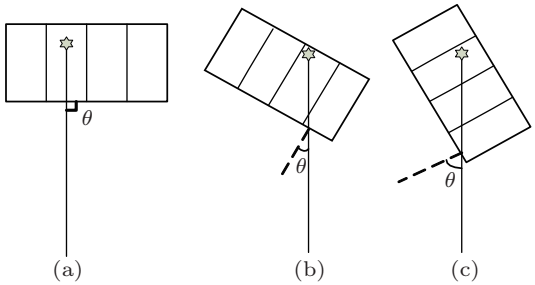


Fig. 2. Three different incidence patterns of gamma-ray: (a) vertical incidence, (b) oblique incidence, and (c) a more oblique incidence.

The incidence angle range in the simulation experiment is set according to that of an existing device. Here, we define the complementary angle of the ordinary incidence angle as the incidence angle for the convenience of calculation (for example θ of Fig. 3). We calculate the incidence angle range for the system geometry of a 64 sided polygon with 11×11 LYSO crystals in each block. The crystal size is 3.5 mm×3.5 mm×15 mm. The gap between two blocks is 4 mm. The incidence angle range of a single photon for the system is 42.7°–90.0° with 353 bins of every angle for the transverse plane. So we can obtain the response of incidence angles from 30° to 90° to satisfy the incidence angles of this scanning system.

We simulate this single photon incidence response mentioned above by Geant4 Application for Emission Tomography (GATE) software based on MC methods.[32] As shown in Fig. 3, in the simulation, a 15×1 LYSO crystal array is set behind a lead collimator. The crystal array is rotated to produce different angles and the lead collimator assures the direction of single incidence. We take 5° for the incidence-angle step from 30° to 90° for the first attempt. The response is obtained based on a probabilistic method. As shown in Fig. 4, by assuming

that N events have been recorded totally, there are n_1, n_2, and n_3 events being recorded in crystal 1, crystal 2, and crystal 3 respectively, so the corresponding probabilities response are n_1/N, n_2/N, and n_3/N.

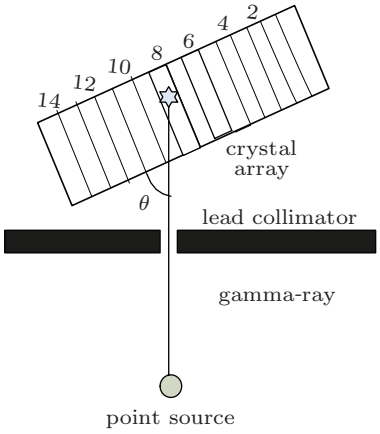


Fig. 3. (color online) The setting of MC simulation of single photon incidence.

Figure 5 displays the responses of the crystal array with two different simulated incidence angles. Figures 5(a) and 5(c) show the original responses. To save the reconstruction time, the probability of each crystal is accumulated along the detected order. If the sum $\geq 80\%$, the probabilities of the other crystals are set to zero and the accounted probabilities are normalized with the sum. Figures 5(b) and 5(d) show the normalized responses. We can see that the gamma-ray at a 60° incidence angle has penetrated more crystals than the gamma-ray at a 90° angle (vertical incidence), which is the same as that obtained in a previous study.[31]

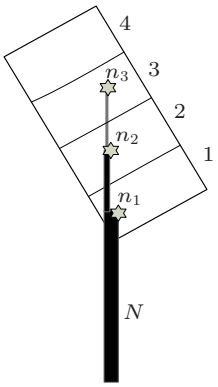


Fig. 4. Probabilistic method for getting the response to single photon incidence.

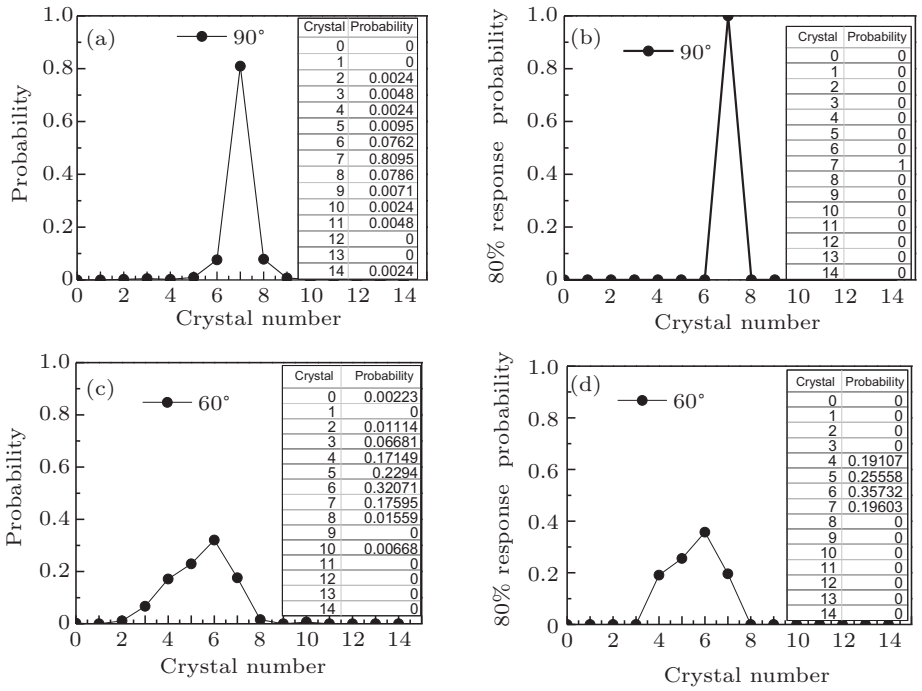


Fig. 5. Single photon incidence response function simulated by MC method. (a) and (c) Original responses at incidence angles of 90° and 60°, respectively. (b) and (d) Normalized responses corresponding to panels (a) and (c). The inset shows the response table.

3.2. Coincidence for PSF–based system matrix

In a PET system, the raw data is acquired from coincidence events of crystal pairs. When a coincidence response is produced from a pair of crystals, single event responses of two crystals are generated simultaneously, so the response signals of the penetrated crystals on two sides would be recorded as a coincidence event for any two crystals, within the coincidence timing window.[31] As shown in Fig. 6, we coincide two back to back single gamma-ray photon responses using the single photon incidence response function in Subsection 3.1

according to this physical process. As shown in Fig. 6, a solid line represents incidence coincidence LOR, and the incidence angles of corresponding crystals b and g are θ_1 and θ_2, respectively. On the side of θ_1, the penetrated crystals are b and c, while on the other side, the penetrated crystals are g, h, and i. Thus, blurrings of coincidence LOR are decided by responses in crystal pairs (b, g), (b, h), (b, i), (c, g), (c, h), and (c, i). We take the product of probability of the two sides penetrated crystals in the single photon response function as the corresponding blurring response probability.[31] Table 1 shows the probabilities of θ_1 and θ_2 in a single photon response function. Crystals b and g are the incident crystals. So, for the incidence of θ_1, the response probabilities of penetrated crystals b and c are p_{11} and p_{12}, respectively, according to Table 1. Similarly, the response probabilities of crystal g, h, and i are p_{21}, p_{22}, and p_{23}, respectively. Table 2 shows the coincident results of the LOR blurring response. Obviously, the LOR blurring response contains both radial and azimuthal blurrings in the transverse plane.[23]

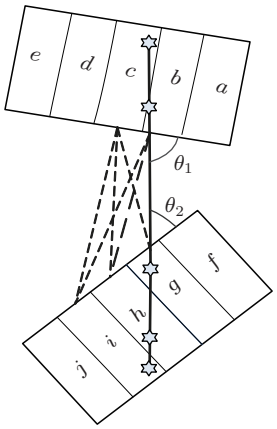


Fig. 6. Coincidence process. The solid line is the incident coincidence LOR, and the dashed lines are the LORs that cause the blurring.

Table 1. Single photon response probabilities of incidence angles θ_1 and θ_2.

Incident angle	Crystal number				
	b	c	g	h	i
θ_1	p_{11}	p_{12}	/	/	/
θ_2	/	/	p_{21}	p_{22}	p_{23}

Table 2. The coincident results of LOR blurring response.

Coincident event	Response probability
Event (b,g)	$p_{11} \times p_{21}$
Event (b,h)	$p_{11} \times p_{22}$
Event (b,i)	$p_{11} \times p_{23}$
Event (c,g)	$p_{12} \times p_{21}$
Event (c,h)	$p_{12} \times p_{22}$
Event (c,i)	$p_{12} \times p_{23}$

To simplify the calculation, we can just calculate a certain number of LOR blurring responses according to the symmetry properties of the PET system geometry.[22]

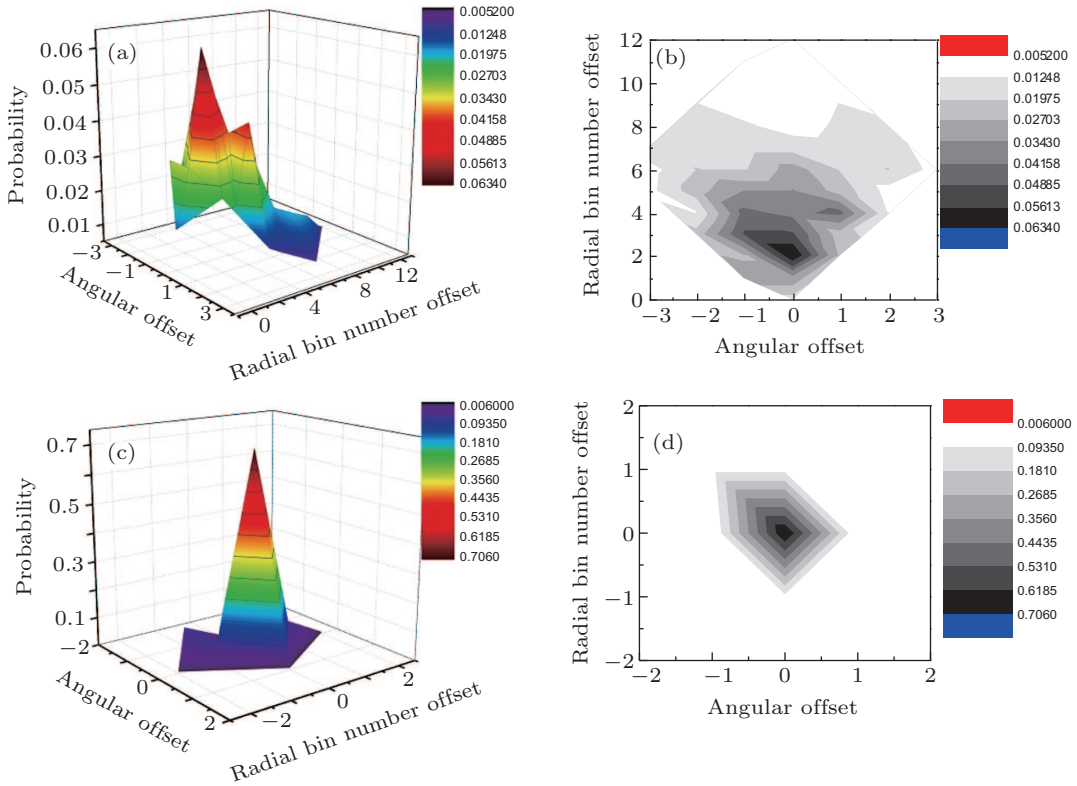


Fig. 7. (color online) The blurring responses of LOR at two different positions in 0° sinogram. We take 353 radial bins in each angle for the scanner. Panels (a) and (b) represent the NO. 1 bin. Panels (c) and (d) represent the NO. 176 bin (the center bin). Panels (a) and (c) present the 3D view of the response. Panels (b) and (d) present the plane view of the response.

Figure 7 shows the coincident results of sinogram (an organizational form of LOR) blurring of two different radial positions at an angle of 0°.We also use a scanner system that has a 64 edge geometry as mentioned above. We can see that the blurring of both positions includes radial blurring and azimuthal blurring. Figures 7(a) and 7(b) represent the response of the furthest bin from the center of the FOV. The bin of the biggest probability has shifted so seriously that the location of the point source will generate a large error in no-PSF reconstruction. The azimuthal response only has some slight blurring, not a large shift.[19] Figures 7(c) and 7(d) are the response of the center bin, which has no serious blurring.

Using sinogram blurring, we can obtain the PSFs of all voxels. We simulate a 64 edge PET system by GATE software and compare the point responses of simulation experimental results between our method and the method without a blurring matrix (the configuration of the PET system is introduced in Section 4). Figure 8 displays this comparison. Figures 8(a)–8(c) show the point response of the center point. The point responses of the simulation experiment, our method, and the ordinary method are similar because of the weak blurring shown in Figs. 7(c) and 7(d). However, at the edge of the FOV in Figs. 8(d)–8(f), the edge bins (the top and the bottom of the sinogram) begin to blur or spread in the point response of the simulation experiment. The point response using our method can describe this blurring spread, while the point response of the ordinary method does not contain the blurring spread.

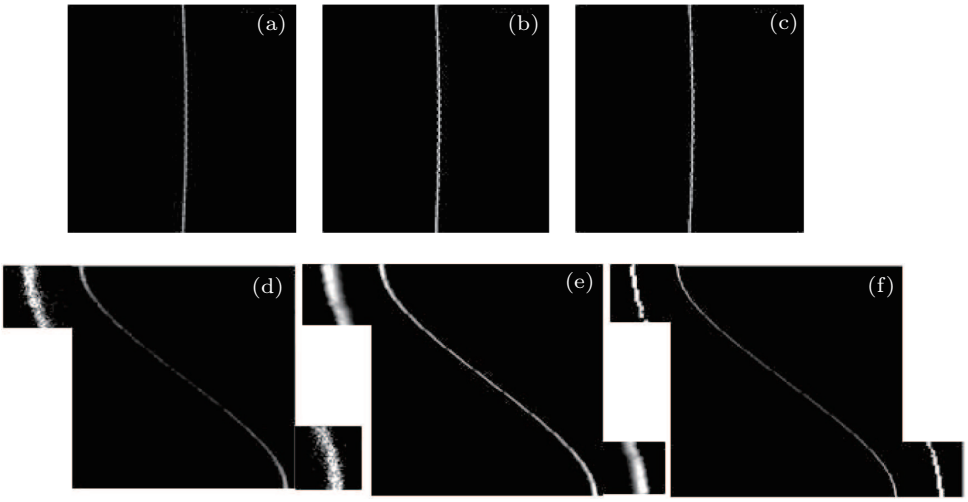


Fig. 8. The point responses of two points for three methods in sonogram. The diameters of the points are 0.5 mm. (a) and (d) Responses from the simulation experiment by GATE software. (b) and (e) Results using our method. (c) and (f) Results of the ordinary method without a blurring matrix. The top row shows the point response of the point placed in the center of the FOV. The bottom row shows the point response of the point placed 300 mm off the FOV center.

3.3. Reconstruction of PSF–OSEM

As a last step, we add the PSF factor into the ordinary geometrical system matrix for both forward projection and back projection by real-time computation to reduce the memory consumption. We use the ordered subset expectation maximization (OSEM) iterative reconstruction[3] to obtain the reconstructed image. In addition, the PSF–OSEM methods consume more computational time than the ordinary OSEM method for the additive spread.

4. Results

The raw data is acquired from both experiments in the system of MC simulation using GATE software and in our whole-body PET imaging experiments (supported by the in-beam whole-body PET, Institute of High Energy Physics, Chinese Academy of Sciences). The scanner systems are both 64 sided polygonals with 64×4 blocks (four blocks in the axial direction). Each block is equipped with 11×11 LYSO crystals whose size is 3.5 mm×3.5 mm×15 mm, as we mentioned above. The gap between every two blocks is 4 mm. The raw data is acquired with a 361–661 keV energy window and a 6 ns timing window. We bin the emission data to a 704×353×87 sinogram matrix after Fourier rebinning.[33] There are 704 angles for every 87 slices and 353 radial bins for each angle in this sinogram matrix.

4.1. Image resolution

Figure 9 shows a comparison of the reconstructed image of the point arrays of PSF–OSEM and ordinary OSEM. The raw data is simulated in the system of MC simulation. The diameter of each point is 0.5 mm. The smallest and the largest distances of the points away from the FOV center are 140 mm and 300 mm, respectively. The distance between every two

points is 20 mm in both radial and tangential directions. The image pixel is 1 mm. In both reconstruction algorithms, eight subsets are used and the reconstructions are stopped after ten iterations. In Fig. 9(a), the OSEM result shows an increased loss of radial resolution as the radial distance increases, while the PSF–OSEM result shows a more uniform radial resolution. Figure 9(b) shows the profiles along the middle row. The curve of points acquired by the OSEM method shows a degeneration of the radial resolution and a larger positional shift of the FOV center, which may result in locating errors.

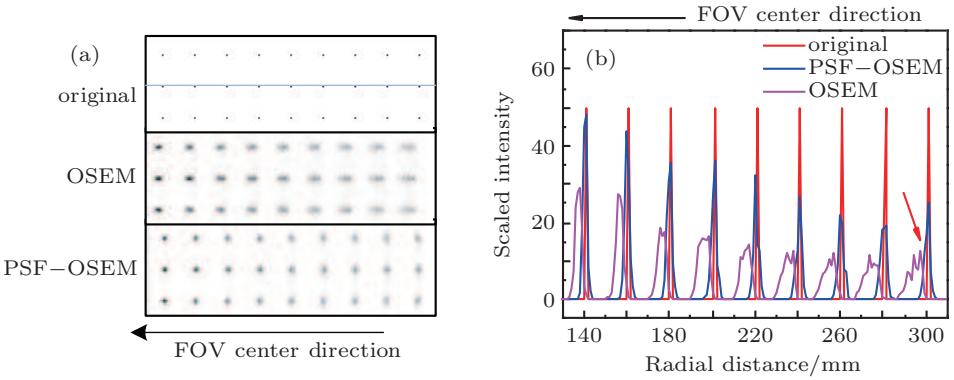


Fig. 9. (color online) The reconstructed image and the middle line profile of the point array generated by MC simulation. The closest point is 140 mm off the center of the FOV, and the furthest point is 300 mm off the center of the FOV. The distance between every two points is 20 mm in both radial and tangential directions. (a) Reconstructed image of the point array. (b) Profile of the middle line points.

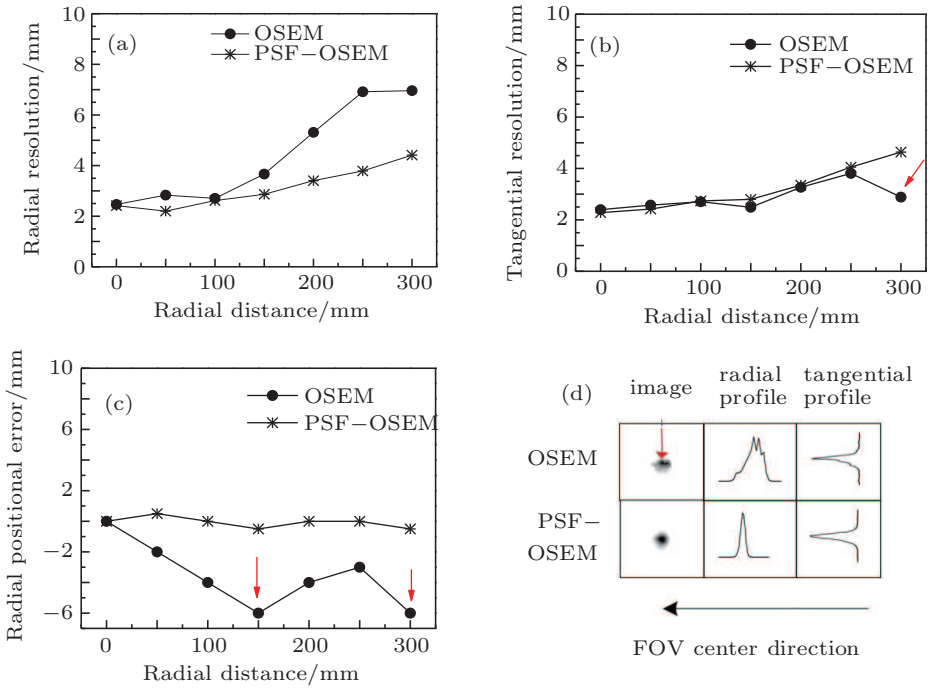


Fig. 10. (color online) (a) Radial resolution, (b) tangential resolution, and (c) radial positional error versus radial distance of single points generated from the system of MC simulation. (d) Reconstructed image of the 300 mm point (the furthest point).

Figures 10(a)–10(c) show the curves of resolution and radial position error versus radial distance. The points are generated singly from the system of MC simulation, according to Section 3 of NEMA Standards Publication.[4] In both reconstruction algorithms, eight subsets are used and the reconstructions are stopped after two iterations. The pixel size is 0.5 mm for the reconstruction. The resolution is specified as the full width at half maximum (FWHM) of the point source response.[4] In Fig. 10(a), the best and the worst radial resolutions for the OSEM results are 2.46 mm and 6.96 mm, respectively, while for the PSF–OSEM, the best radial resolution is 2.42 mm and the worst is 4.41 mm. The radial resolution has been improved in the PSF–OSEM reconstruction. Figure 10(b) shows the similar tangential resolutions in the two methods. The tangential resolution of the point at 300 mm radial distance is sharply lower in the OSEM reconstruction. This is because the furthest point has turned long and narrow or even splits into two or three points because of DOI effects. The profile curve in Fig. 9(b) shows the split of the point at 300 mm radial distance. Figure 10(d) shows the narrow tangential resolution. Figure 10(c) shows the larger error in the radial position for OSEM reconstruction. Most of the points

shift toward the FOV center, and the biggest shift is 6 mm. In Fig. 10(c), the curve also shows a leap (saltus) at 150 mm radial distance and 300 mm radial distance in the OSEM algorithm result, and figure 10(b) shows a sudden slight decrease of the tangential resolution. That is because both positions are at block gap locations where the DOI effects are serious. In contrast, these saltuses are absent from the result of the PSF–OSEM. Table 3 shows the percent of image resolution improvement. We define the percent as

$$I = \frac{R_{\mathrm{OSEM}} - R_{\mathrm{PSF}}}{R_{\mathrm{OSEM}}} \times 100\%. \tag{3}$$

Table 3. Percent of image resolution improvement for simulated data.

Improved item	Radial offset/mm						
	0	50	100	150	200	250	300
Radial resolution	1.9%	22.35%	3.2%	21.8%	35.9%	45.2%	36.6%
Tangential resolution	4.8%	5.9%	–1.1%	–12.4%	–2.5%	–6.4%	–60.8%

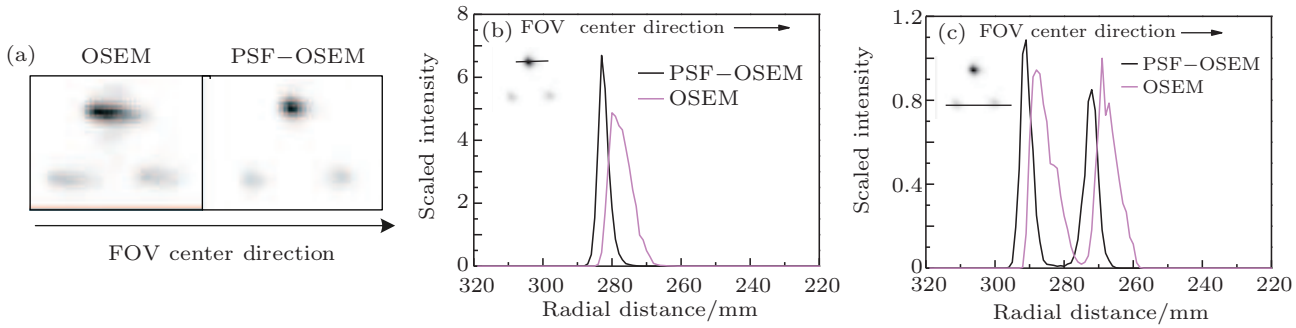


Fig. 11. (color online) The center slice of the reconstructed image of the three rod source data acquired from our PET scanner. The center of the triangle composed of the three rods is at a position 282 mm away from the center of the FOV. (a) The center slice of the reconstructed image. (b) Profile of the top rod of the center slice. (c) Profile of the other two rods of the center slice.

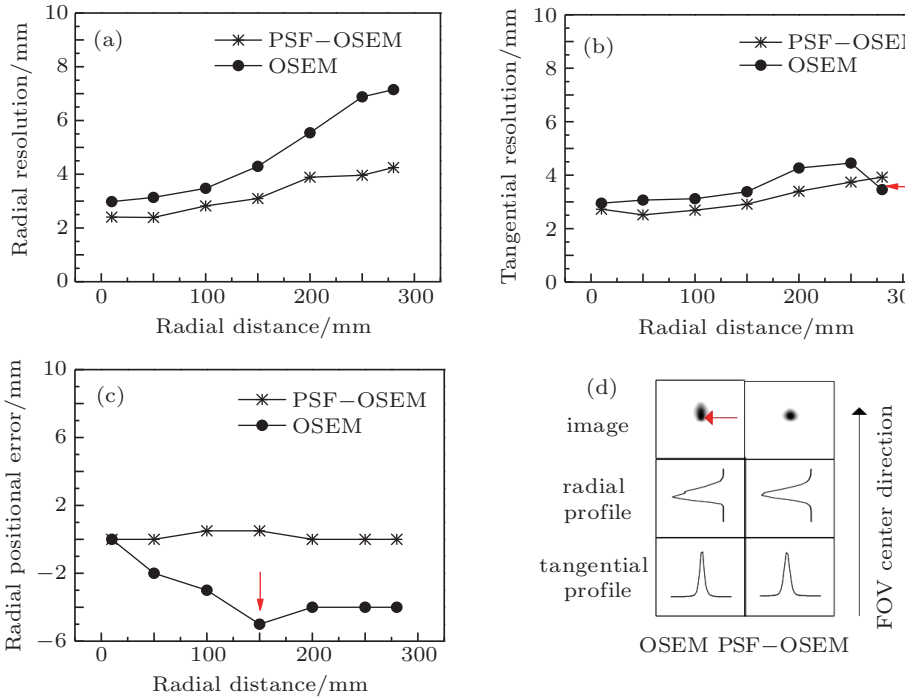


Fig. 12. (color online) (a) Radial resolution, (b) tangential resolution, and (c) radial positional error versus radial distance of the single points data acquired from our PET scanner. (d) Reconstructed image of the 280 mm point (the furthest point).

Table 4. The percent of image resolution improvement for our PET data.

Improved item	Radial offset/mm						
	10	50	100	150	200	250	280
Radial resolution	19.3%	23.8%	18.8%	27.9%	29.8%	42.4%	40.6%
Tangential resolution	7.6%	20%	13.8%	13.8%	20.4%	15.9%	–13.4%

Figures 11 and 12 show the resolution condition of our PET data. In Fig. 11, the activity concentration of the top ^{68}Ge rod source is 3 μCi and that of the other two ^{68}Ge rod sources is 0.5 μCi. The diameter of each rod is 3 mm. The center of the triangle composed of three rods is at a position 282 mm away from the center of the FOV. We use eight subsets, ten iterations, and 1 mm pixel images for both reconstructions. Figures 12(a)–12(c) are curves of image resolution and radial positional error versus radial distance of the single points. The diameter of the 25 μCi ^{22}Na single point is 0.5 mm and the position is configured according to Section 3 of the NEMA Standards Publication.[4] We take eight subsets and two iterations without smoothing in both algorithms. The pixel size is also 0.5 mm according to NEMA Standards Publication.[4] We can come to the same conclusion from both the experimental data and the simulated data. The smallest and the biggest radial resolutions are respectively 2.39 mm and 4.24 mm in the PSF–OSEM result. The corresponding radial resolutions are respectively 2.98 mm and 7.14 mm in the OSEM result. Table 4 shows the percent of image resolution improvement for our PET dada.

4.2. Contrast recovery and noise property

We simulate a sphere phantom in the system of MC simulation. The ratio of activity concentration of hot spheres and background is 8:1. The diameters of the hot spheres are 10 mm, 13 mm, 17 mm, and 22 mm respectively. Figure 13 shows the center transverse slice of the reconstructed image and the center row profile of the two smallest spheres. The raw data is reconstructed by eight subsets and five iterations without smoothing after scatter and attenuation corrections. The image pixel size is 1 mm. Figure 14(a) shows the chosen ROI method. Figures 14(b) and 14(c) show the contrast recovery (hot sphere ROI mean divided by the background ROI mean) curve of the hot spheres and the percent background variability (background ROI std divided by the background ROI mean) curve versus sphere diameter. The percent of background variability is usually used to evaluate the noise property.[4] Table 5 shows the percent of hot sphere contrast recovery and the percent of background variability improvement.

Table 5. Percent of hot sphere contrast recovery and percent of background variability improvement.

Improved item	Sphere diameter/mm			
	10	13	17	22
Hot sphere contrast recovery	26%	11.9%	10.6%	25%
Percent background variability	12.9%	18.1%	8.3%	0%

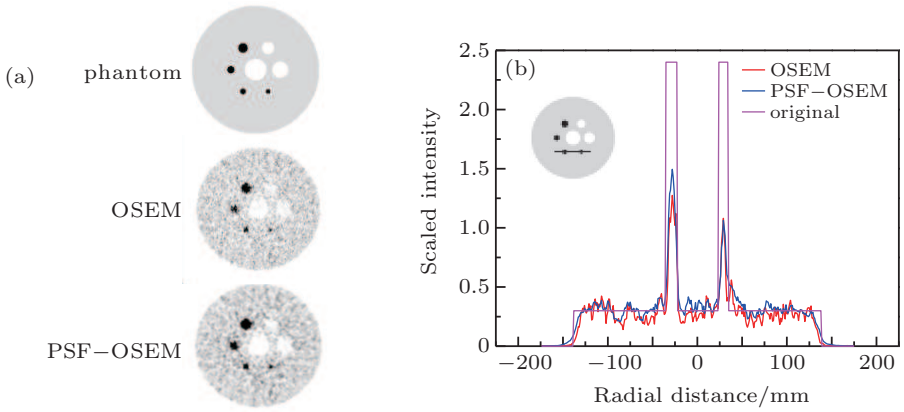


Fig. 13. (color online) Transverse view of the center slice and a profile of the center rows of the two smallest spheres of the sphere phantom, simulated by the system of MC simulation. The ratio of activity concentration of hot spheres and the background is 8:1. The hot spheres' diameters are 10 mm, 13 mm, 17 mm, and 22 mm respectively. (a) Reconstructed image. (b) Profile of the center rows of the two smallest spheres.

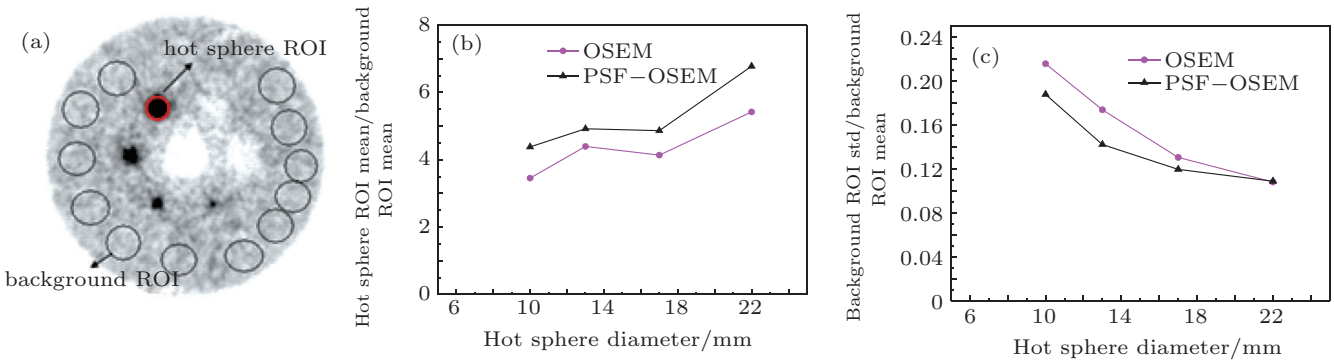


Fig. 14. (color online) (a) The chosen ROI method. (b) Hot sphere contrast recovery (hot sphere ROI mean divided by the background ROI mean) curve versus the sphere diameter. (c) The percent background variability (background ROI standard deviation divided by the background ROI mean) versus the sphere diameter.

5. Discussion and conclusion

In this paper, we have proposed a new method of PSF iterative reconstruction. Our method shows good results, with improved image radial resolution, contrast recovery, and noise property. Moreover, the single photon response function in this method depends on the configuration of crystals instead of the system geometry. With this advantage, we only need to change the coincidence calculation process to adapt to different PET system geometries. However, there are also several problems that need to be discussed here.

5.1. The single photon incidence angle step

In our paper, we choose 5° for the angle step, and the image radial resolution improves inspiringly. If we resize the step to a more proper value, the result will be better. In this paper, we simulate the response by a uniform step. In fact, the response of a single photon penetrating crystals may be non-uniform. The distribution of a single photon penetrating crystals will be studied in future.

5.2. Convergence and computational time

Commonly, the PSF reconstruction converges more slowly than the non-PSF because the PSF contains a lot of blurring information. We must consider how to add some accelerated algorithms (for example, an accelerated algorithm based on GPU) in PSF reconstruction to solve this problem.

5.3. Influence of the nonuniformity of real detector units

The method has assumed that the crystals are uniform. Actually, the cutting technology is relatively mature, and the error among the sizes of the crystals is ± 0.05 mm, Our crystal size in this article is 3.5 mm$\times$3.5 mm, the error is less than 1.4%. We adopt the tube model method to make the system matrix, so this deviation is acceptable.

In addition, we also choose a standard regular polygon to make the system matrix. In reality, we take a rack of regular polygons to assemble the detector structure. The machining error of the rack of regular polygons is less than 0.1 mm, and the assembly error is less than 0.5 mm. If we consider all these errors, the total error of the detector structure is less than 1 mm. In the PET system of our particle, the size of each block is 39.7 mm. So each crystal is in the right place in our model within the margin of error.

References

[1] Gambhir S S, Czermin J, Schwimmer J, Silverman D H, Coleman R E and Phelps M E 2001 *J. Nucl. Med* **42** 1S

[2] Natterer F and Wuebbeling F 2001 *Mathematical Methods in Image Reconstruction* (Vol. 5) (Philadelphia: SIAM) p. 81

[3] Hudson H and Larkin R 1994 *IEEE Trans. Med. Imaging* **13** 601

[4] National Electrical Manufacturers Association 2001 *NEMA Standards Publication NU 2-2001: Performance Measurements of Positron Emission Tomographs* (Virginia: National Electrical Manufacturers Association)

[5] Mawlawi O and Townsend D W 2009 *Eur J. Nucl. Med. Mol. Imaging* **36** S15

[6] Nestle U, Weber W, Hentschel M and Grosu A L 2009 *Phys. Med. Biol.* **54** R1

[7] Pan T and Mawlawi O 2008 *Med. Phys.* **35** 4955

[8] Wiant D B, Gersh J A, Bennett M C and Bourland J D 2009 *Nuclear Science Symposium Conference Record*, October 24–November 1, 2009 Orlando, USA, p. 3758

[9] Chien M K, Yun D, Qing G X and Chin T C 2008 *IEEE Trans. Med. Imaging* **27** 1346

[10] Lecomte R, Schmitt D and Lamoureux G 1984 *IEEE Trans. Nucl. Sci.* **NS-31** 556

[11] Liang Z 1994 *IEEE Trans. Med. Imaging* **13** 314

[12] Rahmim A, Tang J, Lodge M A, Lashkari S, Ay M R, Lautamaki R, Tsui B M W and Bengel F M 2008 *Phys. Med. Biol.* **53** 5947

[13] Alessio A M, Kinahan P E and Lewellen T K 2006 *IEEE Trans. Med. Imaging* **25** 828837

[14] Mumcuoglu E U, Leahy R M, Cherry S R and Hoffman E 1996 *Nuclear Science Symposium, 1996, Conference Record, 1996 IEEE,* November 2–9, 1996 Anaheim, USA, p. 1569

[15] Qi J, Leahy R M, Cherry S R, Chatziioannou A and Farquhar T H 1998 *Phys. Med. Biol.* **43** 1001

[16] Alessio A M and Kinahan P E 2008 *5th IEEE International Symposium on Biomedical Imaging: From Nano to Macro,* May 14–17, 2008 Paris, France, p. 1315

[17] Bernardi E D, Zito F and Baselli G 2007 *Engineering in Medicine and Biology Society, 2007. EMBS 2007. 29th Annual International Conference of the IEEE,* August 22–26, 2007 Lyon, France, p. 6547

[18] Bernardi E D, Zito F, Michelutti L, Mainardi L, Gerundini P and Baselli G 2003 *Engineering in Medicine and Biology Society, 2003. EMBS 2003.25th Annual International Conference of the IEEE,* September 17–21, 2003 Cancun, Mexico, p. 975

[19] Fin L, Bailly P, Daouk J and Meye M E 2009 *Med. Phys.* **36** 3072

[20] Panin V Y, Kehren F, Michel C and Casey M 2006 *IEEE Trans. Med. Imaging* **25** 907

[21] Panin V Y, Kehren F, Rothfuss H, Hu D, Michel C and Casey M E 2006 *IEEE Trans. Nucl. Sci.* **53** 152

[22] Tohme M S and Qi J 2009 *Phys. Med. Biol.* **4** 3709

[23] Alessio A M, Stearns C W, Tong S, Ross S G, Ganin A and Kinahan P E 2010 *IEEE Trans. Med. Imaging* **29** 938

[24] Qi J, Leahy R, Cherry S R, Chatziioannou A and Farquh-ar T 1998 *Phys. Med. Bio.* **43** 1001

[25] Wang L, Wu L W, Wei L, Gao J, Sun C L Chai P and Li D W 2014 *Chin. Phys. B* **23** 2027802

[26] Badawi R D, Lodge M and Marsden P K 1998 *Phys. Med. Bio.* **43** 189

[27] Tohme M S 2011 *Iterative Image Reconstruction for Positron Emission Tomography Based on Measured Detector Response Function Tomography Based on Measured Detector Response Function* (Ph. D. dissertation) (California: University of California)

[28] Joseph P M 1982 *IEEE Trans. Med. Imaging* **MI-1** 192

[29] Johnson C, Yan Y, Carson R, Martino R and Daube-Witherspoon M 1995 *IEEE Trans. Nucl. Sci.* **42** 1223

[30] Chen C, Lee S and Cho Z 1991 *IEEE Trans. Med. Imaging* **10** 513

[31] http://www.opengatecollaboration.org/

[32] Leonard S 2005 *Spatial resolution Study of PET Detector Modules Based on LSO Crystals and Avalanche Photodiode Arrays* (Ph.D. dissertation) (Brussel: Vrije Universiteit Brussel)

[33] Defrise M, Kinahan P, Townsend D, Michel C, Sibomana M and Newport D 1997 *IEEE Trans. Med. Imaging* **16** 145